JOURNAL OF MATERIALS SCIENCE 27 (1992) 1857–1868

Laser-welding behaviour of cast Ni_3Al intermetallic alloy

P. A. MOLIAN, Y. M. YANG
Department of Mechanical Engineering, Iowa State University, Ames, Iowa 50011, USA
T. S. SRIVATSAN
Department of Mechanical Engineering, The University of Akron, Akron, Ohio 44325, USA

Ductile nickel aluminide, $Ni_3Al + B$, is an intermetallic alloy with high strength and ductility making it a promising structural material for both elevated temperature and cryogenic temperature applications. In order to be able to use this alloy over a spectrum of temperature-critical applications, it must be capable of being joined or welded. The weldability of a cast nickel aluminide alloy containing boron was studied using laser welding. Welding was carried out at laser beam traverse speeds ranging from 42.33–254 mm s^{-1} in the bead-on-plate and butt-joint configurations. Two types of surface preparation, namely chemical cleaning and mechanical polishing, were used prior to laser welding. The quality of the laser welds was evaluated through mechanical tests (hardness and tensile), X-ray diffraction and microscopical observations. High-magnification examination of the welds revealed fine columnar structures in the weld zone. The hardness of the weld zone was substantially higher than that of the base metal. Microscopic examination also revealed the welds to contain shrinkage cracks. For a constant set of laser parameters, the chemically etched surfaces provided deeper penetration than the mechanically polished surface. The performance of the laser-welded joint is rationalized.

1. Introduction

Rapid advances in aerospace technology have created a need for a new generation of structural materials. Ordered intermetallic compounds constitute a unique class of metallic materials which have shown promise for replacing conventional nickel-based superalloys. These compounds have been recognized for their superior strength coupled with superior resistance to creep, fatigue and corrosion at elevated temperatures. The chemical ordering in these intermetallic compounds reduces atom mobility at elevated temperatures resulting in good structural stability and resistance to high-temperature deformation [1]. The NiAl and Ni_3Al ordered intermetallic compounds of nickel and aluminium have, in recent years, been the subject of increasing research activity because of their excellent oxidation resistance, fairly high melting temperatures and relatively low densities which make them particularly attractive for potential use as aircraft engine materials.

Nickel aluminide, Ni_3Al, is one of a series of intermetallic compounds of nickel and aluminium having an $L1_2$ ordered crystal structure. The aluminium atoms are ordered on the fcc sites of a unit cell such that each aluminium atom has only nickel atoms for nearest neighbours, forming an $L1_2$ superlattice structure. Alloys based on Ni_3Al are being considered for a spectrum of applications ranging from gas turbines to steam turbines to components used in corrosive environments (oil and gas wells, chemical process industry, marine environments). The Ni_3Al intermetallic compound is of interest for use at elevated temperatures primarily because its yield strength actually increases rather than decreases with increasing temperature up to 750 °C [2–4]. Besides unusual strength behaviour, good creep, oxidation and corrosion resistance have also been identified with this intermetallic compound. However, use of these nickel aluminides, in polycrystalline form, as an engineering material is rendered difficult on account of their low ductility, poor fracture-related properties at ambient temperature and limited fabricability [5–9]. The low ductility and tendency for brittle behaviour was a major obstacle that placed constraints on the development of polycrystalline Ni_3Al alloys and also precluded their use for structural components because of lack of fabricability and fear of premature catastrophic failure. The inferior ductility of the intermetallic compound was attributed to concurrent and competing influences of [10–15]:

(a) an insufficient number of independent slip systems to satisfy the von Mises criterion for general plasticity of a polycrystalline material;
(b) a low cohesive strength of grain boundaries;
(c) embrittling effects of impurities at the grain boundaries; and
(d) a low initial density of mobile dislocations.

In general, techniques for improving the low ductility,

0022–2461 © 1992 Chapman & Hall

inadequate fracture toughness, poor fracture-related properties and fabricability of the ordered intermetallic compound, Ni_3Al, fall into two broad categories:

(i) microstructural modifications through a refinement in grain size and ensuring difficulty in grain boundary crack initiation and propagation;

(ii) compositional modifications through methods of enhancing the probability of $\langle 1\,1\,1 \rangle$ slip by lowering the antiphase energy and/or improving the cohesive strength of grain boundaries. This is particularly important in enhancing the low-temperature ductility of polycrystalline Ni_3Al.

The segregation of impurities to grain boundaries weakens them and promotes premature fracture before macroscopic yield can occur.

In recent years, alloy design efforts have focused on compositional modifications as a means of improving the room temperature ductility and fracture-related properties of Ni_3Al-based alloys. The effects of a small addition of boron to Ni_3Al have been studied by several groups of investigators [13–23]. Interest in the use of boron as a microalloying addition was triggered by an appreciable improvement in the room-temperature ductility of the polycrystalline Ni_3Al alloy due to a change in fracture mode from brittle intergranular to predominantly ductile transgranular fracture in smooth tensile specimens [24]. The change in macroscopic fracture mode was attributed to boron enrichment of grain boundaries as revealed by Auger spectroscopy [20, 21]. The improvement in ductility and fracture properties stimulated research programmes on Ni_3Al alloys and also opened the possibility of practical applications.

The rationale for the present study was to evaluate the weldability characteristics of a polycrystalline Ni_3Al alloy using a high energy-density source. The quality of the laser weld was established through mechanical testing and microscopical observations of the weld. We begin with a brief summary of work done on welding these alloys.

2. Weldability of Ni_3Al alloys

Weldability is a key issue in the development and use of polycrystalline Ni_3Al alloys for a spectrum of applications primarily because joining by conventional welding processes is an important means of fabricating engineering alloys into structural components. In the study of weldments, the following properties are considered: (a) cracks; (b) hardness; (c) strength; and (d) ductility.

Cracking problems do exist in the welding of polycrystalline nickel aluminide (Ni_3Al) alloys. The cracks resulted in fracture propagation occurring from the cracking area, thereby, drastically degrading strength when in service. Previous work has indicated that weld cracking is a major problem for Ni_3Al type alloys [25, 26]. David *et al.* [25] found that crack-free welds were not obtained in polycrystalline Ni_3Al alloys containing boron as an intentional alloying addition. Subsequently, Santella *et al.* [27] found that in gas tungsten arc welding (TIG) and electron-beam welding (EBW) of polycrystalline Ni_3Al alloy, crack-free welds were obtained on wrought materials in the form of sheet and bar. However, crack-free welds were not obtained in castings. The cracking of welds made in castings was attributed to an occurrence of microsegregation effects both in the base material and in the weld zone. The intrinsic effects of microsegregation affected the ordering behaviour of the fusion zone [27].

A study of arc welding and electron-beam welding behaviour of nickel aluminide alloys revealed that (a) composition of the material, and (b) welding speed, affect the susceptibility to cracking. In an earlier study, David *et al.* [25] found that above a certain welding speed, of the order of 13 mm s^{-1}, electron-beam welding of an iron-containing Ni_3Al alloy (IC-25) containing 500 p.p.m. B displayed a strong tendency for cracking in the heat-affected zone (HAZ). Subsequently, Santella *et al.* [26] documented:

(a) the cracks in the heat-affected zone to be intergranular in nature; and

(b) that these cracks formed during solid state transformation.

It was also suggested that the cracks were caused by [28]:

(i) the longitudinal thermal stresses induced during welding; and

(ii) weakening of the grain boundaries at elevated temperatures.

Despite the fact that polycrystalline Ni_3Al-type alloys can be successfully welded by electron-beam welding process over a range of focuses [27], the vacuum requirements in electron-beam welding, during fuel encapsulation, render the process impractical. The innumerable limitations resulting from the use of conventional welding techniques offer laser welding as a suitable alternative to weld these alloys. This attractiveness arises from an ability to transmit the high-power laser beam for appreciable distances, through air at standard pressure, without power attenuation or degradation of optical quality. Furthermore, the laser system produces a concentrated energy source that can be precisely controlled during welding.

Laser welds of iron-, nickel- and titanium-based alloys have shown to exhibit high quality as a result of the following advantages [29]: (a) high processing speeds; (b) high energy density; (c) can be performed in several test environments; (d) an ability to weld difficult materials; (e) no necessity either for electrode or filler materials; (f) narrow welds can be produced; and (g) the heat-affected zone adjacent to the weld is narrow (of the order of 0.3 mm). A brief survey of recently published literature on weldability of Ni_3Al-type alloys reveals that these materials are weldable.

3. Experimental procedure

3.1. Material

The polycrystalline intermetallic alloy used in this study was obtained from Oak Ridge National Laboratory (ORNL). The alloy was designated by ORNL as IC-50. The material was provided in the as-cast condition. The chemical composition of the alloy is listed in Table I, and some physical properties of the

TABLE I Nominal chemical composition (wt %) of the nickel-aluminide (IC-50)

Al	B	Cr	Fe	Mn	Mo	P	Zr	Si	Ni
11.12	0.044	0.046	0.45	0.024	0.002	0.002	0.78	0.03	bal.

TABLE II Some physical properties of IC-50 alloy

Melting point (K)	1663
Density (kg m^{-3})	7500
Specific heat (J kg^{-1} K^{-1})	1414
Thermal conductivity (W m^{-1} K^{-1})	21.37
Thermal diffusivity (m^2 s^{-1})	2.02×10^{-6}

material are summarized in Table II. The as-cast material had two distinct surfaces which were also identified by their colour:

(i) the wheel-contact surface (dark in colour);

(ii) the free-solidifying surface (shining colour surface).

A small section (50.8 mm × 25.4 mm × 1.04 mm) of the as-received material was used in this study. The surfaces of the test specimens were cleaned prior to laser welding. Two cleaning methods were adopted:

(i) mechanical cleaning of the surface with 600 grit silicon carbide abrasive paper; and

(ii) chemical cleaning of the surface with 20% ferric chloride ($FeCl_3$) aqueous solution.

3.2. Laser welding

Two types of laser welding were performed that included bead-on-plate and butt joint. The specimens were mounted on an X–Y table, the motion of which was numerically controlled by a computer. A continuous wave carbon dioxide (CO_2) gas transport laser at a power level of 1.5 kW was used to study the laser weldability of the polycrystalline intermetallic (Ni_3Al) alloy IC-50. The size of the output beam is 19 mm with a Gaussian energy distribution (TEM_{00}). The TEM_{00} mode quality facilitates welding to be performed at high speeds. The laser beam is circularly polarized and was incident normal to the specimen surface. A ZnSe lens with a focal length of 190 mm (7.5 in) was employed to focus the laser beam. Weld travel speed was the key variable in this study.

3.2.1. Bead-on-plate welding

Bead-on-plate welds were made on four specimens:

(a) Specimen 1, mechanically cleaned free-solidifying surface;

(b) Specimen 2, mechanically cleaned wheel-contact surface;

(c) Specimen 3, chemically cleaned free-solidifying surface;

(d) Specimen 4, chemically cleaned wheel-contact surface.

The welds were made using a laser power of 1.5 kW and the laser beam traverse speed was varied from 42.33–254 mm s^{-1}. The laser beam was focused below the specimen surface giving rise to a beam size of approximately 0.5 mm diameter at the surface. Helium gas (at 157 cm^3 s^{-1}) was used to shield the weld from the atmosphere during laser welding.

3.2.2. Butt welding

For butt joints, a single laser pass was made on both sides of the specimen so as to achieve full penetration. The specimens were initially mechanically cleaned. Welds were made using laser power of 1.2 kW and a travel speed of 33.9 mm s^{-1} (80 in min^{-1}). Focusing of the laser beam was below the surface of the specimen such that beam size at the surface measured 1.52 mm diameter. The joint gap for the butt joint was held at 0.016 mm. Nitrogen gas, at about 157 cm^3 s^{-1}, was used for shielding the weld from the atmosphere. The laser parameters for the butt joint were made different from those for bead-on-plate welding in order to get (a) deeper penetration, and (b) to prevent the welds from undercuts. The beam was defocused to a larger size for butt joint than for bead-on-plate weld because the butt joint results in deeper penetration due to effects of absorption for a given set of laser parameters.

3.3. Analysis of welds

Following laser-beam welding, samples from the fusion zone and base metal of the welded specimen were

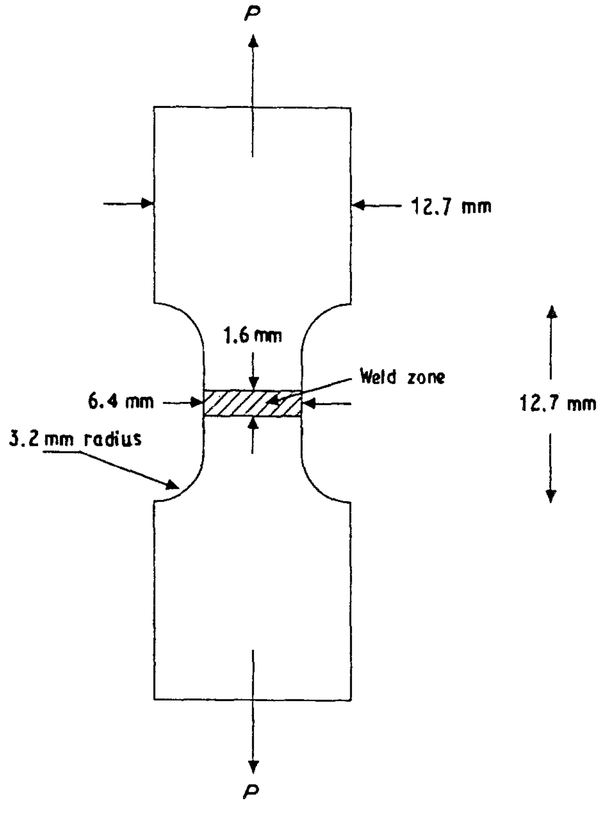

Figure 1 Schematic configuration of the tensile test specimen.

prepared for metallographic observation using standard techniques. The weld samples for observation were sectioned, metallographically polished and etched by swabbing with glyceregia (10 ml nitric acid, 20 ml hydrochloric acid and 30 ml glycerol). A high-resolution optical microscope was used to identify the intrinsic microstructural features and examine the weld quality that included porosity, hot tearing and extent/depth of penetration. X-ray diffraction using a Siemens diffractometer and CuK_α radiation was also used to identify the microstructures.

Tensile and hardness tests were performed on the laser-welded specimens. The tension tests were performed on a closed-loop servohydraulic Universal testing machine at a constant crosshead speed. The test specimen configuration is shown in Fig. 1. The specimens were mechanically polished, cleaned and rinsed in acetone prior to testing. Multiple tests were conducted to ensure consistency in results. A Vicker's microhardness tester was used to determine hardness at various locations along the weld, at a load of 500 g. A scanning electron microscope was used to examine the deformed tensile specimens in order to characterize the predominant fracture mode and the fine scale fracture features.

4. Results and discussion

4.1. Laser welding

Two mechanisms, namely "deep penetration" and "conduction" are involved in laser welding depending on the laser parameters (Fig. 2). A deep-penetration weld is characterized by an hour-glass shape with a high depth to width ratio. Deep penetration is normally accompanied by: (a) excessive melting; (b) loss of material through vaporization; (c) low cooling rate; (d) shrinkage cracks; and (e) gas porosity. These effects are the result of the formation of a "keyhole" with concomitant energy transfer through the keyhole. In contrast, a conduction weld exhibits a small depth-to-width ratio and a low degree of defects. The geometry of a conduction weld is hemispherical and is similar to that of conventional arc welds.

The effect of laser beam traverse speed and prior surface treatment on weld depth (penetration) and weld widths of bead-on-plate (BOP) welds is shown in Figs 3–6. As expected, both weld depth (penetration) and weld width decreased exponentially with laser beam traverse speed, indicating a transition from deep penetration to conduction weld. Deeper penetration and larger widths were observed for the specimens that were chemically cleaned than for the specimens that were mechanically cleaned. This is rationalized on the basis of changes in absorptivity of the laser beam by a modification of chemical and physical nature of both the surface and the subsurface. Chemical cleaning produced chlorides on the surfaces resulting in an increased absorption over the mechanically treated surfaces. Absorption is also a function of several concurrent and competing factors, namely: (a) wavelength; (b) temperature; (c) state of oxidation and corrosion; (d) surface roughness; and (e) electrical resistivity.

A simple energy balance model was used to estimate the absorption coefficient. According to this model [30]

$$P_0 t = 2(C_p \Delta T + L_f)\rho\pi a^2 z \qquad (1)$$

where P_0 is the absorbed laser power $[P(1 - R)]$ (W); P the incident laser power (W), R the reflectivity, t the interaction time (s), C_p the specific heat (J kg K^{-1}), T_m melting temperature (K), T_b ambient temperature (K), L_f the latent heat of fusion (J kg^{-1}), z the depth of penetration (m), and a the beam radius at the surface (m).

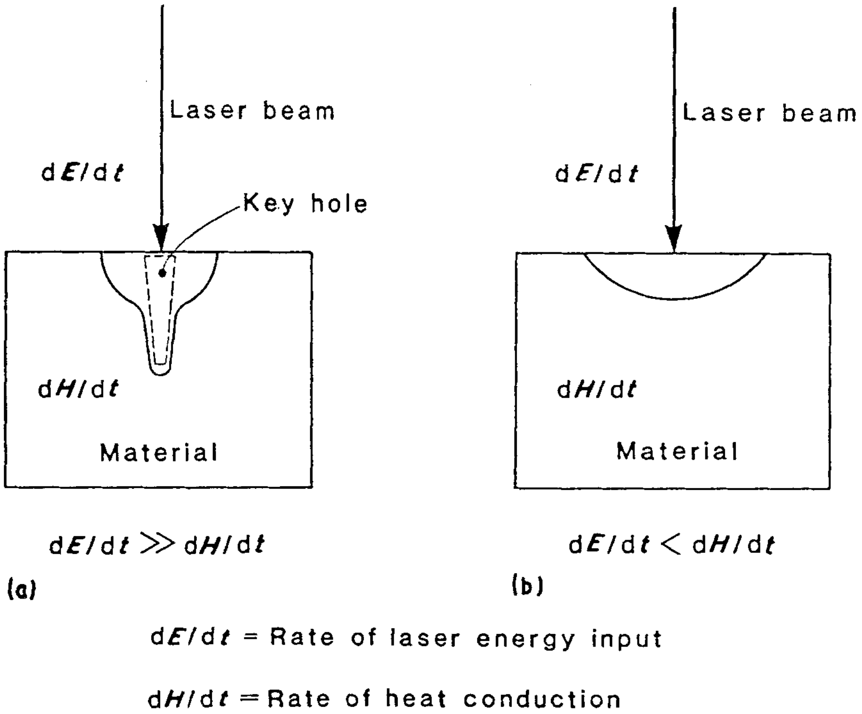

Figure 2 Schematic representation of (a) deep penetration and (b) conduction welds.

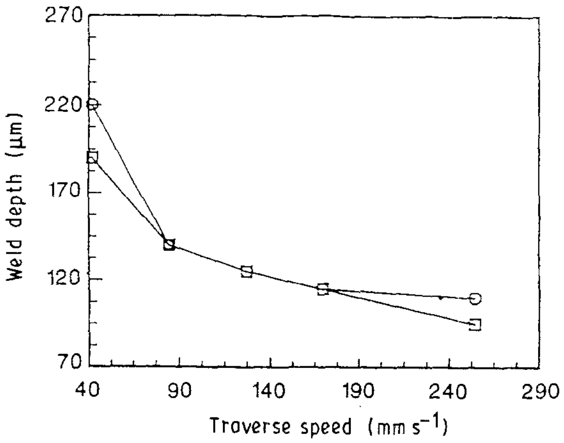

Figure 3 Effect of laser-beam traverse speed on weld depth (penetration) of wheel contact surface. (□) Specimen 2, (○) Specimen 4.

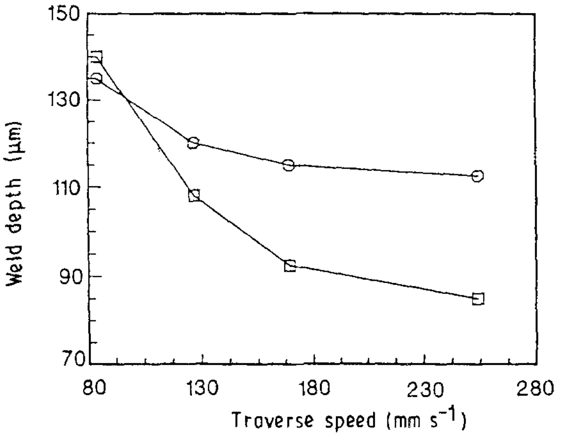

Figure 4 Effect of laser-beam traverse speed on weld depth (penetration) of free-solidifying surface. (□) Specimen 1, (○) Specimen 3.

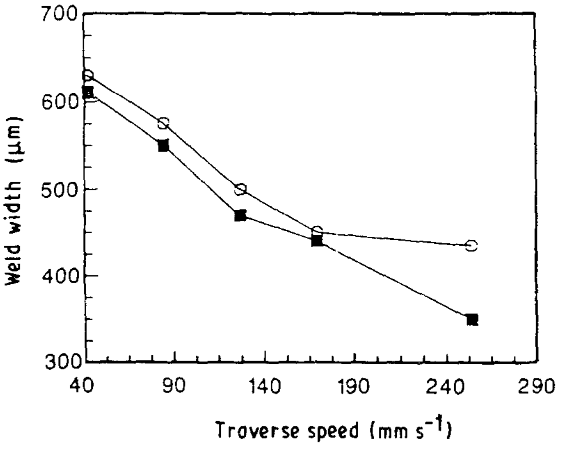

Figure 5 Effect of laser-beam traverse speed on weld widths made on wheel-contact surface. (■) Specimen 2, (○) Specimen 4.

The results of this model are exemplified in Fig. 7. On account of its fine surface finish, a free-solidifying subsurface has lesser absorption than the wheel-contact subsurface. It is thus clear that the absorption of laser energy, in conduction-limited welds, is determined by the nature of both the surface and the subsurface.

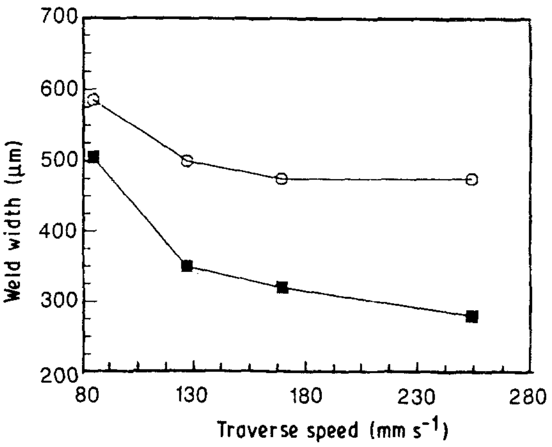

Figure 6 Effect of laser-beam traverse speed on weld widths made on free-solidifying surface. (■) Specimen 1, (○) Specimen 3.

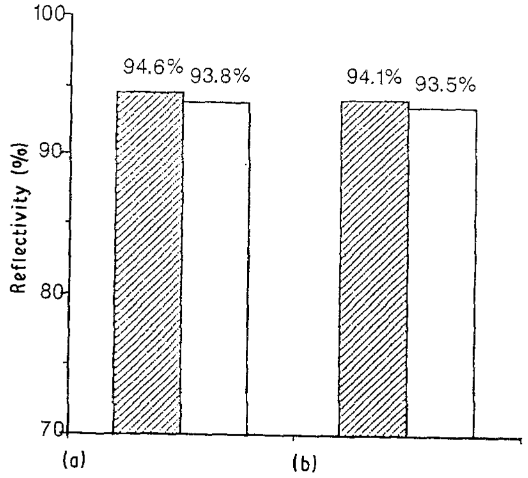

Figure 7 Comparison of type of surface cleaning on reflectivity: (a) free-solidifying surface; (b) wheel-contact surface. (▨) Mechanically cleaned, (□) chemically cleaned.

Representative transverse sections of weldments showing the conduction-limited fusion zones are given in Figs 8 and 9. Fine microcracks were evident in all the welds. The tendency for microcracking and the fineness of a crack increased with an increase in laser-beam traverse speed. Variation of weld cracking frequency with laser-beam traverse speed is provided in Fig. 10. This Figure also reveals that chemical cleaning of the surface produced more microcracks than mechanical cleaning. The increased cracking is attributed in part to the formation and presence of chlorides that contribute to enhancing brittleness.

An insight into the effect of beam traverse speed on weldability can be obtained by considering the influence of this variable on the thermal cycles experienced by the weldment [31, 32]. High beam traverse speeds produce high heating and cooling rates. These in turn create steep thermal stress gradients in both the fusion zone and the heat-affected zone. The rapid thermal cycles reduces the total time available for thermally activated processes to occur. At low beam-traverse speeds the temperature gradients in the heat-affected zone normal to the fusion line are relatively small and

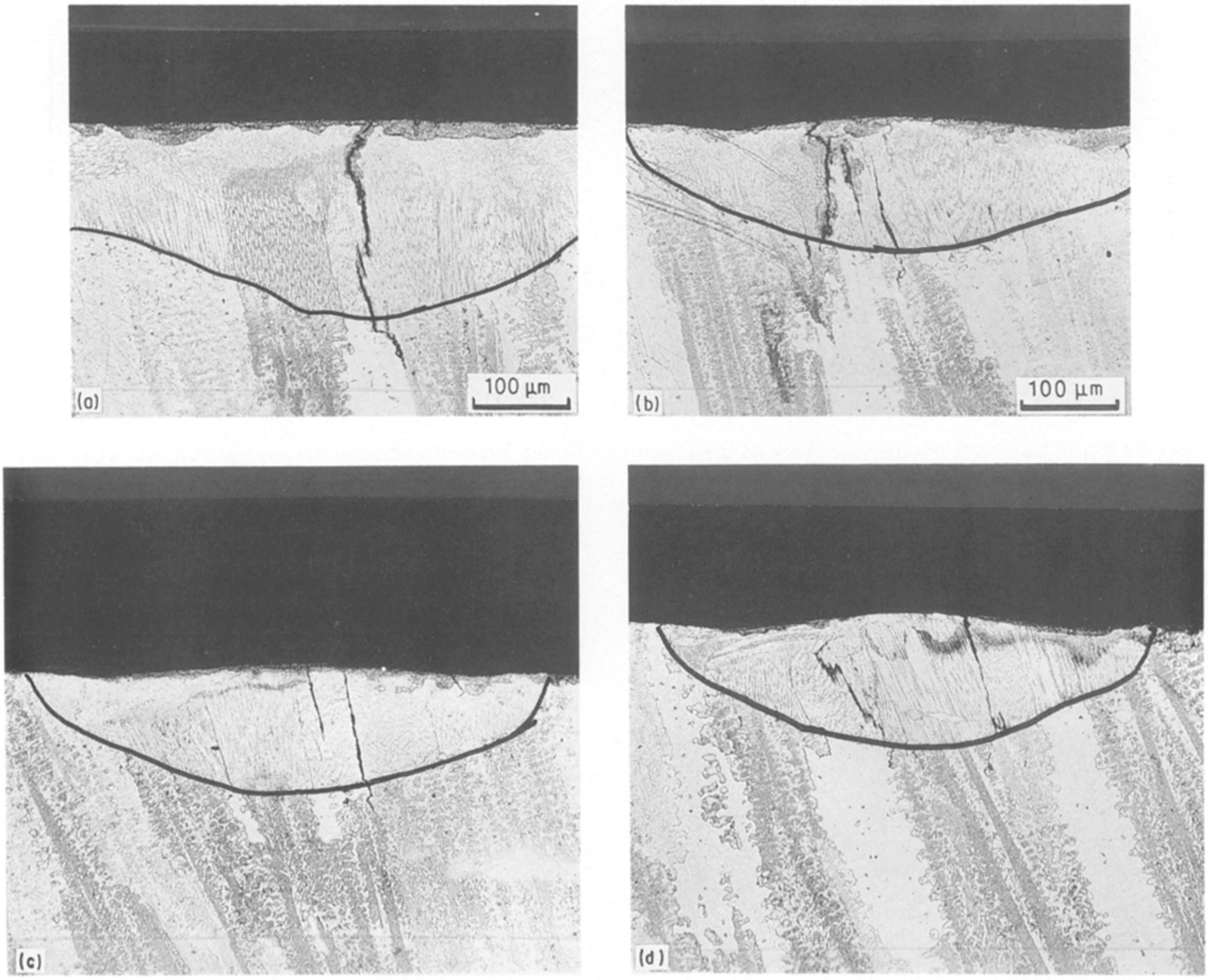

Figure 8 Optical micrograph of transverse section of chemically cleaned free-solidifying surface test specimen at: (a) welding speeds of (a) 42.3 mm s^{-1}; (b) 84.67 mm s^{-1}; (c) 169.3 mm s^{-1}; and (d) 254 mm s^{-1}.

change progressively with time. However, temperature gradients in both the fusion zone and the heat-affected zone are large at high welding speed. Also, high beam traverse speeds tend to:

(a) localize stresses due to steep thermal gradients in the heat-affected zone; and

(b) produce intrinsic stress distributions that change rapidly with time.

Thermal stress analyses of arc welding indicates that for a point in the heat-affected zone close to the fusion line, the longitudinal compressive stresses build-up with approach of the arc, and reverses to tensile stress once the arc has passed [32]. It seems plausible that this factor contributes to localization of stresses which eventually exceeds the fracture strength of the material at the temperature. It was noted by Santella *et al.* [33] that possible degradation in ductility with changes in temperature may also contribute to the observed cracking problem during welding. The addition of boron to an ordered intermetallic alloy provides several beneficial effects including enhanced elevated temperature strength and improved ductility, thereby, facilitating fabrication. However, the presence of boron contributes to conditions that lead to a loss of hot ductility in the fusion zone and the heat-affected zone [34]. This can be related to an intrinsic melting occurring at the local level coupled with microcracking in the fusion and heat-affected zones.

Although boron tends to segregate preferentially to grain boundaries in boron-doped nickel aluminides [35], no localized melting was observed in the heat-affected zone of the polycrystalline Ni_3Al alloy (IC-50) studied. However, a ductility minimum at elevated temperatures associated with solute segregation effects coupled with intrinsic grain boundary weakness promotes cracking. Laser-beam welds made on the polycrystalline Ni_3Al alloy revealed fine intergranular cracks in the fusion zone. In an earlier study, it was shown by Huang *et al.* [36] through X-ray diffraction analysis of Ni_3Al, that the lattice parameter of boron-containing polycrystalline Ni_3Al-type alloys increased monotonically with boron concentration. However, in the present study the lattice parameter measured at the wheel-contact surface was found to be greater than the lattice parameter measured on the non-contact (free-solidifying) surface. Therefore, boron concentration at the wheel-contact surface was higher than that at the free-solidifying surface. The cracking severity of polycrystalline Ni_3Al alloys was shown to increase with boron concentration [25, 26]. Consequently, the welds made on the free-solidifying surface, which contains less boron, are less prone to microcracking than

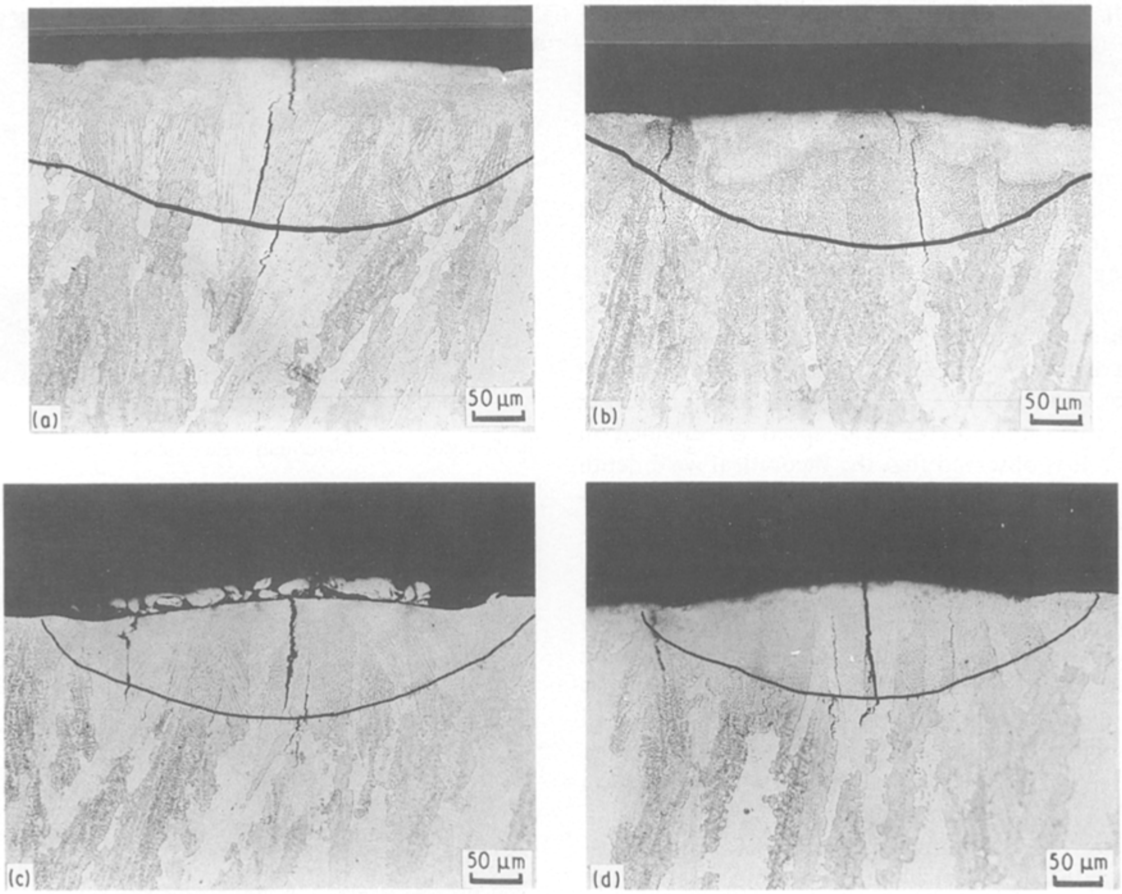

Figure 9 Optical micrograph of transverse section of chemically cleaned wheel-contact surface specimen at: welding speeds of (a) 42.3 mm s^{-1} (b) 84.67 mm s^{-1}; (c) 169.3 mm s^{-1}; and (d) 254 mm s^{-1}.

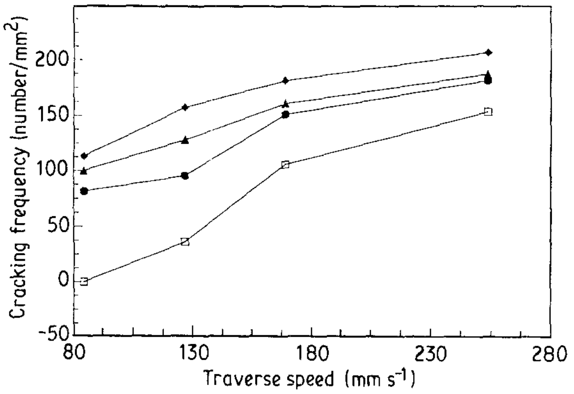

Figure 10 Variation of weld cracking frequency with laser-beam traverse speed. (□) Specimen 1, (●) Specimen 2, (▲) Specimen 3, (◆) Specimen 4.

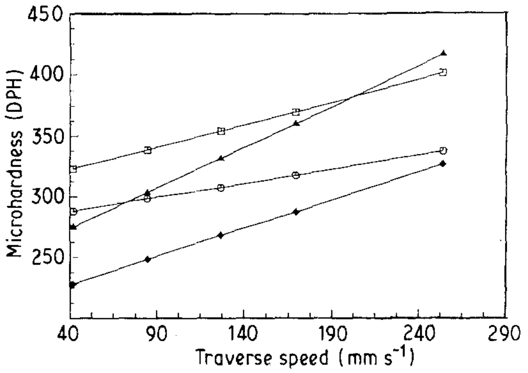

Figure 11 Variation of weld zone microhardness with beam traverse speed (welding speed). (□) Specimen 1, (○) Specimen 2, (▲) Specimen 3, (◆) Specimen 4.

welds made on the wheel-contact surface. This observation is consistent with results shown in Fig. 10.

Variation of microhardness with laser-beam traverse speed is shown in Fig. 11. It is observed that the microhardness increased with beam traverse speed. Whies *et al.* [37] found the hardness of a polycrystalline nickel aluminide alloy doped with boron to reflect an Hall–Petch character of the flow stress. According to their theory, the hardness of an intermetallic alloy can be expressed as [37]

$$H = H_0 + k_d d^{-0.5} \qquad (2)$$

where d is the grain size. An increase in fineness of the microstructures resulted from an increase in beam traverse speed, as shown in Figs 8 and 9. Therefore, it is concluded that a higher beam traverse speed provides a finer fusion zone structure resulting in higher hardness value in this zone.

The penetration depths and weld widths of conduction-limited welds can be estimated by solving the heat flow equation given by Carslaw and Jaeger for various conditions [38]. Assuming the laser beam to be a line source of heat moving rapidly through an infinitely wide thin plate (heat flow is two dimensional), the temperature distribution is given by [38]

$$T - T_0 = \frac{P_0}{2\pi k z}\exp(X)K_0(R) \qquad (3)$$

where T is the temperature at any point (K), T_0 the ambient temperature (K), P_0 the absorbed power (W), k the thermal conductivity ($\mathrm{W\,m^{-1}\,K^{-1}}$), z the weld depth (m), X a dimensionless parameter ($vx/2$), v the welding speed ($\mathrm{m\,s^{-1}}$), k the thermal diffusivity ($\mathrm{m^2\,s^{-1}}$), K_0 the Bessel function of second kind and zeroth order, and R a dimensionless parameter.

For a beam diameter of 0.5 mm at the specimen surface, and considering $T = T_m$, the variation of weld depth as a function of weld speed is provided in Fig. 12. It is observed that the theoretical weld depth accords well with the experimental data. This observation suggests that it is reasonable to consider heat conduction effects based on an absorptivity of the surface. A typical fusion zone of the butt-weld is shown in Fig. 13. Intergranular cracks were apparent in the fusion zone (Figs 13 and 14). The cracking behaviour of the as-received polycrystalline alloy (IC-50) suggests that the material does not have very good weldability. A better understanding of the cracking behaviour of the alloy can be had from the work of Liu *et al.* [35]. These researchers showed the tensile ductility of boron-containing Ni_3Al alloys to be dramatically reduced as the aluminium concentration approached or exceeded 25 at %. It is reasonable to expect a similar effect of stoichiometry on ductility of the IC-50 alloy studied. Boron was found to preferentially occupy aluminium sublattice sites in Ni_3Al alloys. Therefore, it is plausible that grain-boundary segments in the as-cast polycrystalline Ni_3Al alloy are relatively brittle and, consequently, have reduced capacity for accommodating the stresses arising from welding.

At a traverse speed of 33.8 $\mathrm{mm\,s^{-1}}$ (80 in $\mathrm{min^{-1}}$) the shape of the weld is a tear-drop. In such cases, only a few grains survive and grow towards the centreline, thereby, leading to a coarse columnar structure in the fusion zone. A structure of this kind is more prone to cracking. Furthermore, a coarse grain structure results in reduced grain-boundary contact area for a given amount of non-equilibrium liquid during welding. Hence, the presence of coarse-grained structures in the fusion zone renders it more susceptible to solidification cracking than with fine-grained structures. A scanning electron micrograph of the fractured fusion zone is shown in Fig. 14. This micrograph confirms the existence of intergranular cracks in the fusion zone and these cracks are attributed to intrinsic solidification effects.

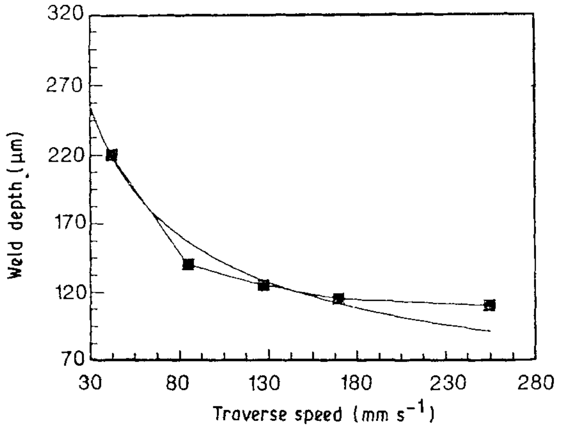

Figure 12 Comparison of (■) experimental weld depth (Specimen 4) with (——) estimated weld depth using Carslaw and Jaeger's heat flow theory.

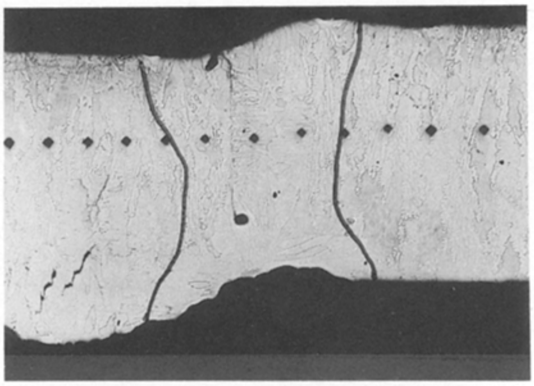

Figure 13 Optical microstructure showing intergranular cracking in the fusion zone of laser-butt weld of alloy IC-50.

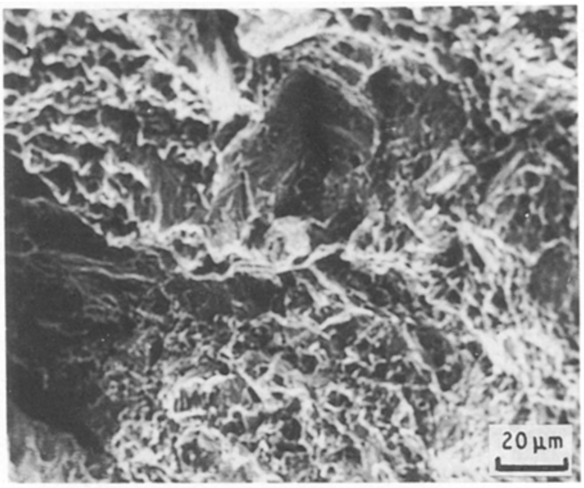

Figure 14 Scanning electron micrograph showing intergranular cracks in the fusion zone.

The microstructure of the fusion zone and the base metal are shown in Figs 15 and 16. Both the fusion zone and the base metal contain a small amount of the γ' phase dispersed in the matrix (γ). Although laser welding resulted in a coarse columnar grain structure in the fusion zone, it is obvious that the columnar grains in the fusion zone are relatively finer than those in the base metal. Fig. 17 shows the X-ray diffraction pattern obtained from laser-beam welded sample and the base material. It is observed that in both the laser-beam welded (LBW) sample and the base material, the diffraction peaks of (1 0 0) and (2 0 0) from the $L1_2$ structure are higher than other texture peaks. This indicates the formation and presence of a strong (1 0 0) series texture in the IC-50 alloy. The textures were slightly stronger in the laser-beam welds than in the base material. The observed zone axis was consistent

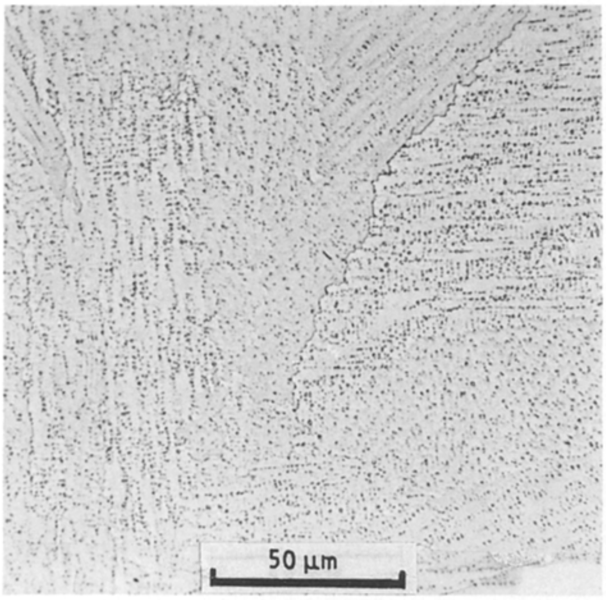

Figure 15 Optical micrograph showing microstructure of the fusion zone of the polycrystalline $Ni_3Al + B$ alloy (IC-50).

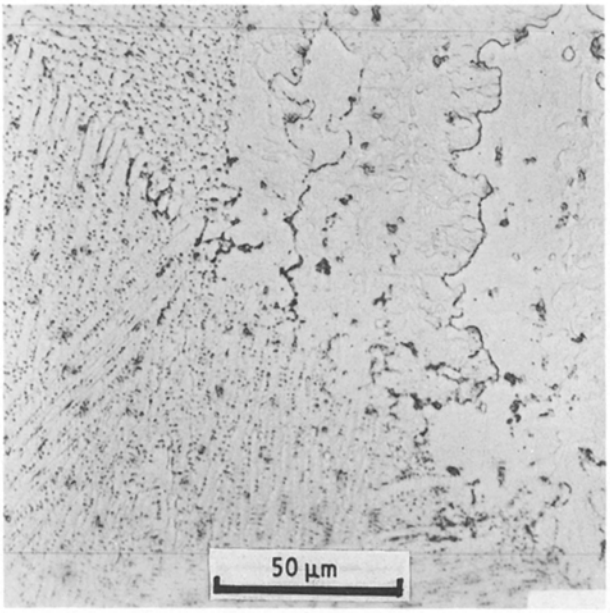

Figure 16 Optical micrograph showing microstructure of the base material.

with those observed in nickel-based superalloys and in $(NiHf)_3Al$ [39]. Both the nickel-based superalloy and the $(NiHf)_3Al$ alloy showed [1 0 0] growth direction during directional solidification of single crystals. Similar diffraction patterns from the laser-beam welded (LBW) sample and the base material indicates that laser beam welding of the IC-50 alloy retained the stable ordered $L1_2$ structure even under conditions of non-equilibrium solidification encountered during laser welding.

A microhardness traverse was conducted on the laser welds and results are shown in Fig. 18. The microhardness of the base metal averaged 270 DPH. The maximum hardness (315 DPH) was achieved in the fusion zone. The increased hardness in the fusion zone is attributed in part to the refinement in grain structure.

The results of ambient temperature tensile test on alloy IC-50 weldments are summarized in Table III, along with tensile properties of the base material for comparison. The orientation of the test specimens was such that the weld axis was perpendicular to the tensile axis. A comparison of the engineering stress–engineering strain curves of the weldment and the base metal is made in Fig. 19. It is obvious from the stress–strain curves that strength properties of the

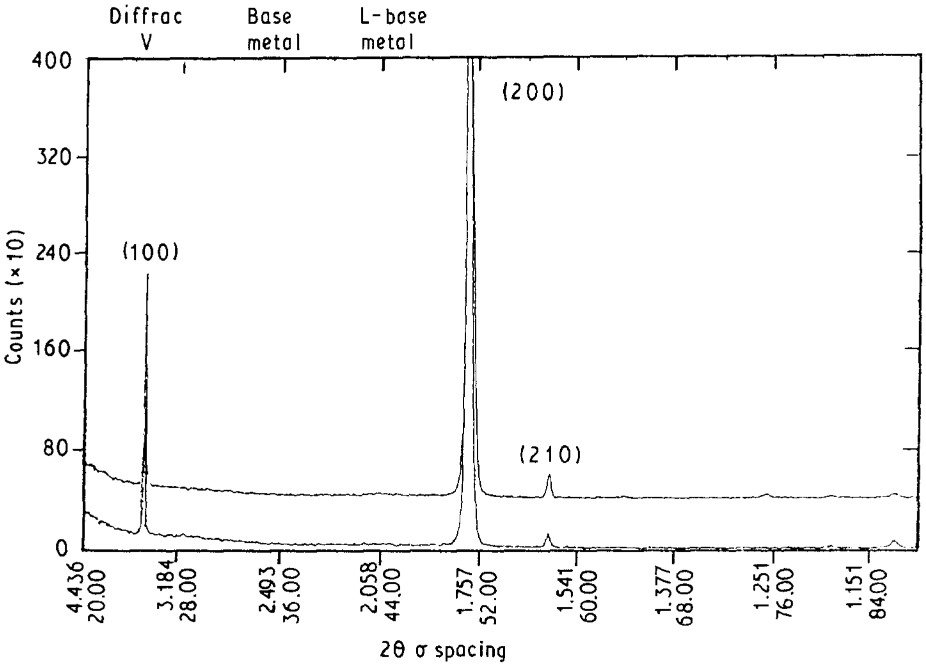

Figure 17 X-ray diffraction patterns from the laser-welded zone and the base material. The upper line is the diffraction pattern from the laser weld zone, while the bottom line is the diffraction pattern from the base material.

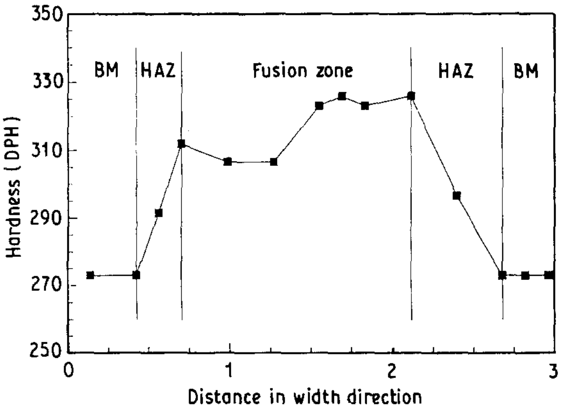

Figure 18 Microhardness profile across the fusion zone, heat-affected zone and the base metal.

TABLE III Comparison of tensile properties of LBW IC-50 and base material

	Laser-beam weld	Base material
Yield strength (MPa)	314	348
Ultimate strength (MPa)	677	809
Elongation (%)	39	58
Area reduction (%)	32	44

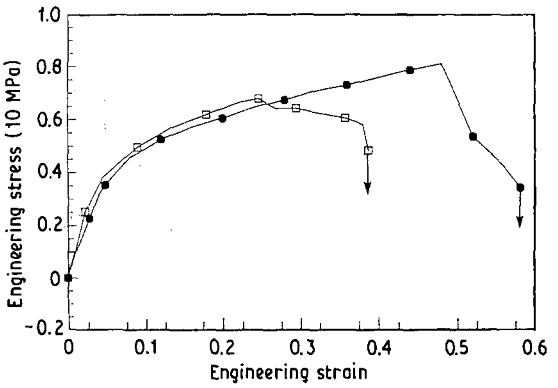

Figure 19 Comparison of engineering stress–engineering strain curves of (■) the base metal and (□) the laser-beam weld.

weldments are comparable to strength of the base metal. However, ductility of the weldment was inferior to that of the base metal.

Scanning electron microscopy observations of the tensile fracture surfaces was conducted to elucidate information on fracture mode and mechanism. The general morphology of the cracked surface is shown in Fig. 20. In an earlier study on this alloy system, it was suggested that the loss in ductility can be reduced by minimizing the normal stresses across grain boundaries [40]. If the normal stress is held below a critical level, the cracks would neither nucleate at grain-boundary regions nor would they propagate through or along the grain boundaries. The normal stress, σ_N, across a grain boundary in a specimen subjected to an applied stress, σ, is equal to

$$\sigma_N = \sigma \cos^2 \theta \qquad (4)$$

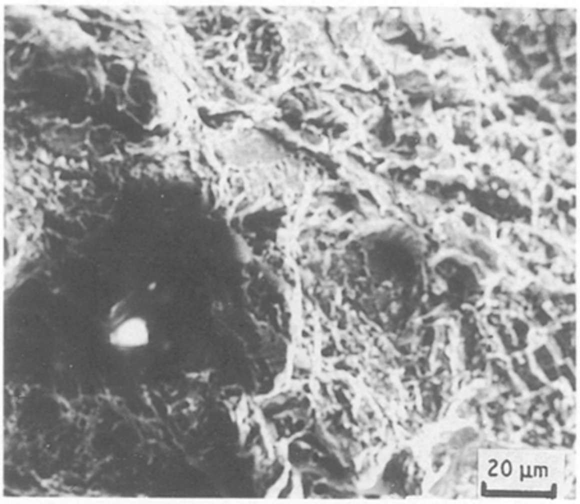

Figure 20 Scanning electron micrograph showing fracture characteristics of the fusion zone.

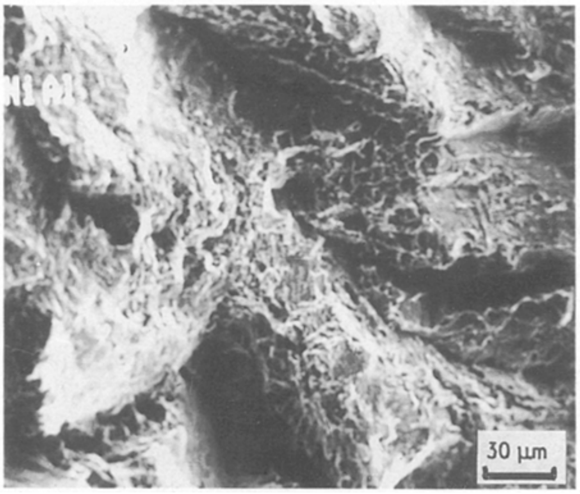

Figure 21 Scanning electron micrograph of the fractured weld showing ductile microvoid coalescence in the fusion zone.

where θ is the angle between the grain-boundary normal and the tensile axis. The columnar grain structure with vertical grain boundaries (i.e. $\theta \approx 90°$) minimizes the normal stress. Consequently, microcracks cannot be readily initiated at and along the grain boundaries. Furthermore, even if a microcrack forms at an inclined grain boundary on the specimen surfaces, the motion of the crack is impeded by the neighbouring grain boundary because of the difficulty associated in propagating the crack along such a boundary. This is a plausible reason for the improved strength-related properties of the laser-beam weldment even though it contained cracks in the fusion zone. The good-to adequate ductility properties of the weld tensile specimens can be attributed, in part, to failure (or the fusion zone) by ductile microvoid coalescence (Fig. 21). The ductile transgranular fracture mode is shown in the scanning electron micrographs, Figs 22 and 23. These micrographs reveal the overall fracture appearance of both the laser-beam welded specimen and the base material, at high magnification. The laser-beam welded specimen exhibits bimodal

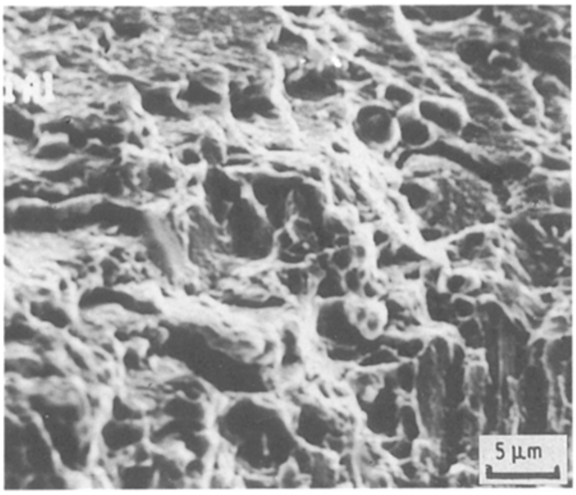

Figure 22 Scanning electron micrograph of the laser-beam weld zone showing predominantly transgranular fracture.

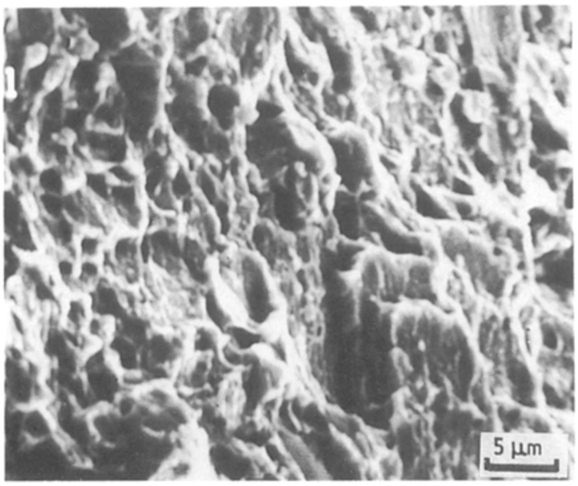

Figure 23 Scanning electron micrograph of the base material.

failure with predominantly transgranular fracture regions associated with traces of "cleavage" like features along certain crystallographic planes (Fig. 22). Tensile fracture of the base material was predominantly transgranular. The transgranular fracture surfaces were covered with shallow equiaxed dimples (Fig. 23). The fracture surface morphology suggests that the existence of stress concentration in the laser-beam weld (LBW) zone is higher than that in the base material. Consequently, the higher stress concentration degrades the ductility of the laser beam weld (LBW) specimens (39%) in comparison with the base material (58%).

5. Conclusions

The general conclusions of the present study on the weldability of the nickel aluminide intermetallic IC 50 are summarized as follows.

1. Absorption characteristics of the laser beam can be enhanced by prior surface treatment. Chemical cleaning of the test specimen surface resulted in deeper penetration than mechanical cleaning.

2. Weld cracking was found to be influenced by the type of surface treatment and the subsurface condition. The susceptibility to microcracking increased with an increase in laser beam traverse speed.

3. The increased hardness of the laser welds is attributed to the highly concentrated heat input of the laser beam and the high traverse speeds which resulted in a refinement in the grain structure in the fusion zone and the heat-affected zone.

4. Ambient temperature tensile properties of the laser-beam weldments were comparable with properties of the base material, although there existed cracks in the fusion zone. Intrinsic stress concentration effects along the grain boundary of the laser-welded zone contribute to the observed loss in ductility.

5. X-ray diffraction revealed diffraction peaks of (1 0 0) series textures from the $L1_2$ structure to be higher than other texture peaks. Laser-beam welds of the alloy revealed a similar diffraction pattern as the base material indicating that they retained the ordered $L1_2$ structure even under conditions of non-equilibrium solidification during welding.

Acknowledgements

This work was partially supported by the Iowa State University, and the University of Akron through Faculty Research Grant (no. 1058). The authors thank Dr Vinod K. Sikka, Oak Ridge National Laboratory and Programme Monitor of this programme for providing the material used in this study.

References

1. M. H. YOO, J. A. HORTON and C. T. LIU, *Acta Metall.* **36** (1988) 2935.
2. P. A. FLINN, *Trans TMS AIME* **218** (1960) 145.
3. R. G. DAVIS and N. S. STOLOFF, *ibid.* **233** (1965) 714.
4. E. A. AITKEN, "Intermetallic Composites" (Wiley Interscience, New York, 1967) pp. 491–50.
5. E. M. GRALA, "Mechanical Properties of Intermetallic Composites" (Wiley Interscience, New York, 1960) p. 358.
6. R. MOSKOVICH. *J. Mater. Sci.* **13** (1978) 1901.
7. A. V. SEYBOLT and J. H. WESTBROOK, *Acta Metall.* **12** (1967) 449.
8. K. AOKI and O. IZUMI, *Trans. Jpn Inst. Metals* **19** (1978) 203.
9. G. W. GROVES and A. KELLY, *Phil. Mag.* **8** (1963) 877.
10. T. P. WEIHS, V. ZINOVIEV, D. V. VIENS and E. M. SCHULSON, *Acta Metall.* **35** (1987) 1109.
11. M. S. KIM, S. HANNADA, S. WATANABE and O. IZUMI, *J. Jpn Inst. Metals* **52** (1988) 1020.
12. S. V. RAJ, R. D. NOEBE and R. BOWMAN, *Scripta Metall.* **23** (1989) 2049.
13. C. T. LIU, C. L. WHITE and J. A. HORTON, *Acta Metall.* **33** (1985) 213.
14. C. T. LIU and C. L. WHITE, *ibid.* **35** (1987) 643.
15. C. T. LIU, *Mater. Res. Soc. Symp. Proc.* **81** (1987) 355.
16. A. I. TAUB, S. C. HUANG and K. M. CHANG, *Metall. Trans. A* **15A** (1984) 399.
17. A. I. TAUB, S. C. HUANG and K. M. CHANG, *Mater. Res. Soc. Symp. Proc.* **39** (1985) 221.
18. A. I. TAUB, K. M. CHANG and C. T. LIU, *Scripta Metall.* **20** (1986) 1613.
19. I. BAKER, E. M. SCHULSON and J. A. HORTON, *Acta Metall.* **35** (1987) 1533.
20. C. L. WHITE, R. A. PADGETT, C. T. LIU and S. M. YALISOVE, *Scripta Metall.* **18** (1984) 1417.

21. A. CHOUDHURY, C. L. WHITE and C. R. BROOKS, *ibid.* **20** (1986) 1061.
22. J. J. LEWANDOWSKI, C. A. HIPPSLEY, M. B. D. EFFIS and J. F. KNOTT, *Acta Metall.* **35** (1987) 593.
23. P. S. KHADKIKAR, J. J. LEWANDOWSKI and K. VEDULA, *Metall. Trans.* **20A** (1989) 1247.
24. M. S. KIM, S. HANADA, S. WATABABLE and O. IZUMI, *J. Mater. Sci.* **25** (1990) 1590.
25. S. A. DAVID, W. A. JEMIAN, C. T. LIU and J. A. HORTON, *Weld. J.* **64** (1) (1985) 22s.
26. M. L. SANTELLA and S. A. DAVID, *ibid.* **65** (5) (1986) 129s.
27. M. L. SANTELLA, J. A. HORTON and S. A. DAVID, *ibid.* **67** (3) (1988) 63s.
28. M. L. SANTELLA, M. C. MAGUIRE and S. A. DAVID, *ibid.* **68** (1) (1989) 19s.
29. J. MAZUMDER, *J. Metals* **7** (1982) 16.
30. JOHN F. READY, "Industrial Applications of Lasers" (Academic Press, New York, 1978).
31. W. R. APBLELL and W. S. PELLINI, *Weld. J.* **1** (1956) 83s.
32. S. KOU and Y. LEE, *Metall. Trans.* **14A** (1983) 2245.
33. M. L. SANTELLA, S. A. DAVID and C. L. WHITE, in "High Temperature Ordered Intermetallic Alloys", edited by C. Koch, C. Liu and N. S. Stoloff (Materials Research Society, Pittsburgh, 1985) pp. 495–503.
34. W. A. OWCZARSKI, D. S. DUVALL and C. P. SULLIVAN, *Weld. J.* **45** (4) (1966) 1456.
35. C. T. LIU, C. L. WHITE, C. C. KOCH and E. H. LEE, in "Proceedings of Symposium in High Temperature Materials Chemistry", Vol. II. Edited by Z. A. Munzir (Electrochemical Society, Pennington, 1983) pp. 32–41.
36. S. C. HUANG, A. I. TAUB, K. M. CHANG and C. L. BRIANT and D. L. HALL, *Rapidly Quenched Metals* (1985) 1407.
37. T. P. WHIES, V. ZINOVIEV, D. V. VIENS and E. M. SCHULSON, *Acta Metall.* **35** (1987) 1109.
38. H. S. CARSLAW and J. C. JAEGER, "Conduction of Heat in Solids", 2nd Edn (Oxford University Press, 1959).
39. R. S. BELLOWS and J. K. TIEN, *Scripta Metall.* **21** (1987) 1659.
40. C. T. LIU and B. F. OLIVER, *J. Mater. Res.* **4** (2) (1989) 294.

Received 6 December 1990
and accepted 13 May 1991